

Radiative conductivity and abundance of post-perovskite in the lowermost mantle

Sergey S. Lobanov^{1,2,*†}, Nicholas Holtgrewe^{1,3,†}, Jung-Fu Lin^{4,5}, Alexander F. Goncharov^{1,6}

¹Geophysical Laboratory, Carnegie Institution of Washington, Washington, DC 20015, USA

²V.S. Sobolev Institute of Geology and Mineralogy SB RAS, Novosibirsk 630090, Russia

³Howard University, 2400 Sixth Street NW, Washington, DC 20059, USA

⁴Department of Geological Sciences, Jackson School of Geosciences, The University of Texas at Austin, Austin, TX 78712, USA

⁵Center for High Pressure Science and Technology Advanced Research (HPSTAR), Shanghai 130012, China

⁶Key Laboratory of Materials Physics, Institute of Solid State Physics CAS, Hefei 230031, China

*Corresponding author: slobanov@carnegiescience.edu

†These authors contributed equally to this work

Abstract

Thermal conductivity of the lowermost mantle governs the heat flow out of the core energizing planetary-scale geological processes. Yet, there are no direct experimental measurements of thermal conductivity at relevant pressure-temperature conditions of Earth's core-mantle boundary. Here we determine the radiative conductivity of post-perovskite at near core-mantle boundary conditions by optical absorption measurements in a laser-heated diamond anvil cell. Our results show that the radiative conductivity of $\text{Mg}_{0.9}\text{Fe}_{0.1}\text{SiO}_3$ post-perovskite ($< 1.2 \text{ W/m/K}$) is $\sim 40\%$ smaller than bridgmanite at the base of the mantle. By combining this result with the present-day core-mantle heat flow and available estimations on the lattice thermal

conductivity we conclude that post-perovskite is as abundant as bridgmanite in the lowermost mantle which has profound implications for the dynamics of the deep Earth.

Main text

The lowermost 200-400 km of the mantle is a critical region responsible for the core-mantle interaction powering all major geological processes on Earth¹. Specifically, thermal conductivity of the thermal boundary layer (TBL) above the core-mantle boundary (CMB) determines the heat flow out of the core that provides energy to sustain the mantle global circulation and to drive the geodynamo^{1,2}. Seismic structures of the lowermost mantle, however, are complex^{3,4} implying that the thermal conductivity of the region is non-uniform due to variations in chemical (*e.g.* iron) and/or mineralogical contents as well as texturing of the constituting minerals. The nature of the seismic heterogeneity near the CMB, including a sharp increase in shear wave velocity and anti-correlations of seismic parameters, has been linked to the bridgmanite (Bdgm) to post-perovskite (Ppv) transition^{5,6}, as these phases have contrasting elastic, rheological, and transport properties (*e.g.* Ref.⁶). Indeed, measurements and computations of lattice thermal conductivity (k_{lat}) in Bdgm and Ppv revealed that Ppv conducts heat 50-60 % more efficiently than Bdgm^{7,8}, suggesting that the distribution of the Ppv phase can significantly enhance the heat flux out of the core. However, no mineral physics constraints are available on the radiative thermal conductivity (k_{rad}) of Ppv, which should play an increasingly important role at high temperature⁹, as well as on the Ppv abundance in the lowermost mantle. This has hampered our understanding of how the heat flux across the CMB may vary laterally and what magnitude of the energy source in the mantle and the outer core is needed to power their convections.

Previous estimates of radiative thermal conductivity at lower mantle conditions were based on high-pressure room-temperature measurements of the absorption coefficients of representative minerals in the mid/near-infrared and visible spectral range¹⁰⁻¹⁴. The presence of

an intense thermal radiation emitted from the hot sample makes measurements of the optical properties at high temperatures relevant to the lowermost mantle (approximately 3000 K) very challenging as common light sources have similar radiative temperatures. In the absence of the experimental data, the effect of temperature was neglected. It has been argued that temperature-induced variations in the absorption spectrum of Bdg are small as intensity of the crystal-field band is determined by a symmetry distortion of the $\text{Fe}^{2+}\text{O}_{12}$ -polyhedra in Bdg¹². However, the intensity of the crystal field spectrum in iron-bearing minerals can be sensitive to pressure, temperature, iron concentration, and iron spin states^{10, 15-19}. Moreover, due to a substantial amount of Fe^{3+} in Bdg and Ppv at lower mantle conditions^{20, 21}, the absorption coefficients and thus the radiative conductivity of these minerals are also governed by the Fe^{2+} - Fe^{3+} charge transfer (CT)¹⁵, which is expected to diminish with temperature²². Therefore, to ascertain the presently unknown radiative conductivity of iron-bearing minerals at expected CMB conditions, it is of fundamental importance to underpin physical mechanisms that govern optical absorption of lower mantle minerals at simultaneous high pressure-temperature conditions. It is also desirable to assess the intensity of the absorption bands as a function of the total iron content because the solubility of iron in lower mantle minerals can vary with pressure, temperature, and phase/spin transitions²³.

In this work we have studied optical properties of iron-rich, Fe^{3+} -bearing Ppv ($\text{Mg}_{0.6}\text{Fe}_{0.4}\text{SiO}_3$) at 300-2050 K and 130 GPa using laser-heated diamond anvil cells combined with a pulsed ultra-bright supercontinuum probe (400-2400 nm) synchronized with the collection windows of gated visible and infrared detectors. The latter allowed diminishing the contribution of thermal radiation to the optical signal at high temperature by several orders of magnitude. We determined quantitatively the reduction in intensity of all Ppv absorption bands in the visible-infrared range at high pressure and temperature. These, in turn, have allowed us to constrain the spin and valence states of iron in Ppv and its radiative conductivity at expected CMB conditions. Combined with literature data on the absorption coefficients of Bdg and ferropericlase (Fp),

these results enable us to construct a radiative thermal conductivity model for the lowermost mantle in order to address the CMB heat flux and Ppv content in the region.

Iron-rich ($\text{Mg}_{0.6}\text{Fe}_{0.4}\text{SiO}_3$) Ppv was synthesized in a diamond anvil cell using enstatite powder of the corresponding composition sandwiched between NaCl layers, similar to procedures used in previous reports on the spin and valence states in Ppv²⁴. The sample was compressed to 130 GPa at room temperature and then laser heated at 2500-2800 K for 6-8 hours at 13IDD beamline of GSECARS, Advanced Photon Source. The synthesis was confirmed by synchrotron x-ray diffraction that showed a complete transformation to the Ppv phase. After successful synthesis of Ppv, analysis of the measured room-temperature absorption spectrum in the 6000-22500 cm^{-1} range shows three distinct features at energies typical for crystal field and CT transitions (Fig. 1)¹⁵.

The band assignment of our absorption spectra is based on first-principles calculations at zero Kelvin^{25,26} and is consistent with experimental room-temperature Mössbauer data collected previously on samples with similar synthesis conditions²⁴, providing necessary reference information on the identification for the iron spin and valence states in Ppv at 300 K (see Supplementary Materials). Specifically, low spin (LS) Fe^{3+} occupies the 6-fold B-site (Supplementary Fig. S1), while the 8-fold A-site is occupied by both high spin (HS) Fe^{3+} and HS Fe^{2+} . Combining these results with Tanabe-Sugano diagrams for d^5 and d^6 elements we deduce the spin-allowed electronic transitions in the crystal field of iron in Ppv at 130 GPa and 300 K: ${}^5\text{E}_g \rightarrow {}^5\text{T}_{2g}$ in A-site HS Fe^{2+} and ${}^2\text{T}_{2g} \rightarrow {}^2\text{T}_{1g}$ (${}^2\text{A}_{2g}$) in B-site LS Fe^{3+} . Importantly, all crystal field transitions in HS Fe^{3+} are spin-forbidden.

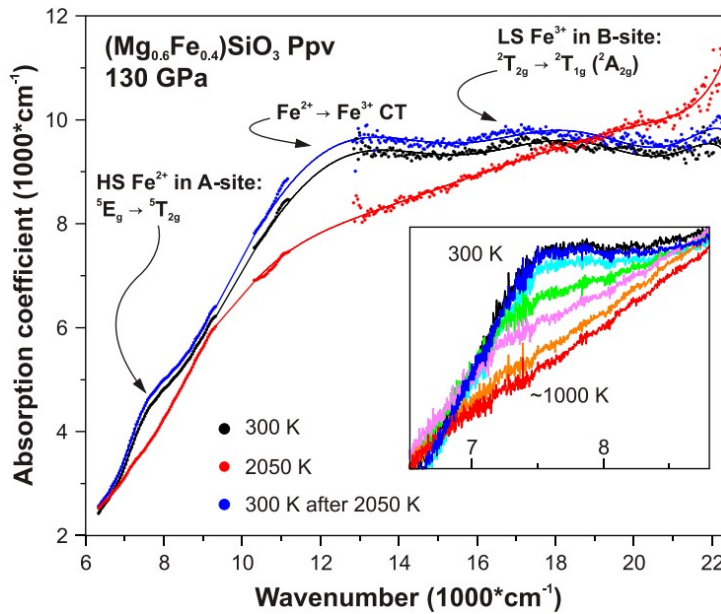


Figure 1. Absorption coefficients of Ppv with $\text{Mg}_{0.6}\text{Fe}_{0.4}\text{SiO}_3$ composition at 130 GPa. Black: before heating; red: at ~ 2050 K; blue: quenched to room temperature. Spectral regions that lack absorbance data are due to the need to block the spectral range ($9500\text{-}10500\text{ cm}^{-1}$) near the heating laser wavelength (1070 nm) and the limited sensitivity of the iCCD and InGaAs detectors at $11000\text{-}13000\text{ cm}^{-1}$. Lines are fits to the spectra to guide the eye. Inset: temperature-induced changes in the $6500\text{-}8700\text{ cm}^{-1}$ range at $T = 300$ (black and blue) to ~ 1000 K (red). All observed transformations are reversible.

The band centered at $\sim 7500\text{ cm}^{-1}$ is assigned to the ${}^5\text{E}_g \rightarrow {}^5\text{T}_{2g}$ transition in HS Fe^{2+} at the A-site based on the relatively weak crystal field splitting energy of its 8-fold coordination (see Supplementary Materials). Upon laser-heating, the ${}^5\text{E}_g \rightarrow {}^5\text{T}_{2g}$ band red-shifts and weakens continuously with increasing temperature to $T \sim 1000$ K (Fig. 1). Interestingly, the red-shift represents a typical behavior of a crystal field band due to the thermal expansion decreasing the crystal field splitting energy. The vanishing intensity, however, is highly uncommon for single-ion crystal field bands¹⁵. Likewise, the band intensity is not scaled linearly with the Ppv iron content (Supplementary Fig. S2), as would be expected for single-ion crystal field bands, suggesting that the absorption of light by the A-site HS Fe^{2+} is enhanced by interactions with the edge-sharing B-site Fe^{3+} . Indeed, exchange-coupling interactions of adjacent transition metal ions have been employed to explain the anomalous temperature and concentration behavior of

the crystal field bands^{27,28}. However, the importance of this transition mechanism for the absorption coefficient of lower mantle minerals has been previously overlooked. Alternatively, the disappearance of the band at $T \sim 1000$ K may indicate that the ${}^5E_g \rightarrow {}^5T_{2g}$ band becomes parity-forbidden due to temperature-induced static and/or dynamic distortions imposing a center of symmetry to the A-site (vibronic decoupling)¹⁵. A detailed crystallographic analysis of intensities and positions of multigrain Bragg reflections may allow discriminating between these two hypotheses. In the absence of such information we assume the exchange-coupled mechanism plays a dominant role in the intensity weakening.

The band centered at 17500 cm^{-1} is assigned to the ${}^2T_{2g} \rightarrow {}^2T_{1g}$ (${}^2A_{2g}$) transition in LS Fe^{3+} at the B-site as it corresponds to the lowest energy spin-allowed excited state of d^5 elements (Supplementary Fig. S3 and Supplementary Materials). At 2050 K, the LS Fe^{3+} band is no longer observed (Fig. 1), indicating a temperature-induced LS to HS transition at expected P - T conditions of the CMB. In Al-bearing BdgM all iron is likely accommodated by the 12-folded A-site and remain in the HS state at lower mantle P - T (Refs.²⁹), as opposed to Fp which may contain a significant portion of LS iron (up to 50 %) at the bottom of the lower mantle³⁰. Accordingly, Fp is the only major host of LS iron in the lower mantle.

The most prominent spectral feature observed here is the broad absorption band at 12000 - 13000 cm^{-1} (Fig. 1) which we assign to a Fe^{2+} - Fe^{3+} CT transition. This band is characteristic of mixed-valence compounds¹⁵ and has an increased bandwidth compared to crystal field bands¹⁵. The decreased intensity at high temperature supports this assignment because the number of absorbing Fe^{2+} - Fe^{3+} pairs in the ground state (N) decreases with temperature (T) as $N \sim 1 - \exp(-E_a/kT)$, where E_a is the activation energy for a thermally-induced CT and k is the Boltzmann constant. Additionally, Fe^{2+} -O and Fe^{3+} -O CT (absorption edge) may give rise to the intense absorption in the spectrum at frequencies above 22000 cm^{-1} (Fig. 1; Supplementary Fig. S2).

A conventional approach to assess k_{rad} for a given room temperature absorption coefficient (α) is:

$$k_{rad}(T) = \frac{4n^2}{3} \int_0^\infty \frac{1}{\alpha(\nu)} \frac{\partial I(\nu, T)}{\partial T} d\nu \quad (1)$$

where n is the refractive index of a given mineral, ν is frequency, and $I(\nu, T)$ is the Planck function^{11, 12}. As revealed in this study, the absorption coefficient of Ppv is controlled by a number of physical mechanisms such as the temperature-activated spectroscopic selection rules and temperature-inhibited magnetic coupling. It follows that most accurate values of k_{rad} require absorption coefficients evaluated at high temperature. Unlike previous studies of lower mantle k_{rad} (Refs.¹⁰⁻¹⁴), we determined the efficiency of the radiative heat transfer mechanism at high temperature based on the 2050 K absorption data. The comparison based on the 300 and 2050 K data (Supplementary Fig. S4) reveals that the effect of temperature-dependent absorption coefficient on k_{rad} is on the order of 10 %, in spite of the substantial changes in the absorption spectra (Fig. 1). The relative difference tends to get smaller with increasing temperature due to the diminishing overlap of the blackbody radiation with Ppv absorption. As the refractive index of Ppv at 130 GPa is unknown, we assume a wavelength-independent value of $n = 2.1$, based on a density-corrected refractive index of Bdgm³¹. We estimated a combined uncertainty of ~ 25 % in k_{rad} due to uncertainties in determination of both sample thickness and refractive index (see methods).

The radiative conductivity of the lowermost mantle is determined by absorption coefficients of its constituting materials likely including Ppv, Bdgm, and Fp. To construct a model of radiative conductivity in the TBL we used previously reported room-temperature absorption coefficients of Ppv ($\text{Mg}_{0.9}\text{Fe}_{0.1}\text{SiO}_3$)¹⁹, Bdgm ($\text{Mg}_{0.9}\text{Fe}_{0.1}\text{SiO}_3$)¹³, and Fp ($\text{Mg}_{0.85}\text{Fe}_{0.15}\text{O}$)¹³. As revealed in this study (Supplementary Fig. S4), the use of 300 K Ppv absorption coefficients underestimates k_{rad} by ~ 10 % at CMB conditions ($P \sim 135$ GPa and $T \sim 4000$ K). To address the effect of iron substitution on radiative conductivity, we applied the 10 %

correction determined in this work to k_{rad} values inferred from the 300 K absorption data of Ppv with variable iron content (10-30 %) reported by Goncharov et al.¹⁹ (Fig. 2 inset), assuming that iron-depleted Ppv exhibits a similar temperature-dependence of the absorption coefficient. Given the similarities in iron valence and spin distribution between the A- and B-sites in the structures of Bdgm and Ppv (Refs.^{25,26}), one may expect that the light absorption mechanisms in Bdgm have an analogous temperature-dependence to that in Ppv. Accordingly, we applied the same 10 % upward correction to Bdgm radiative conductivity.

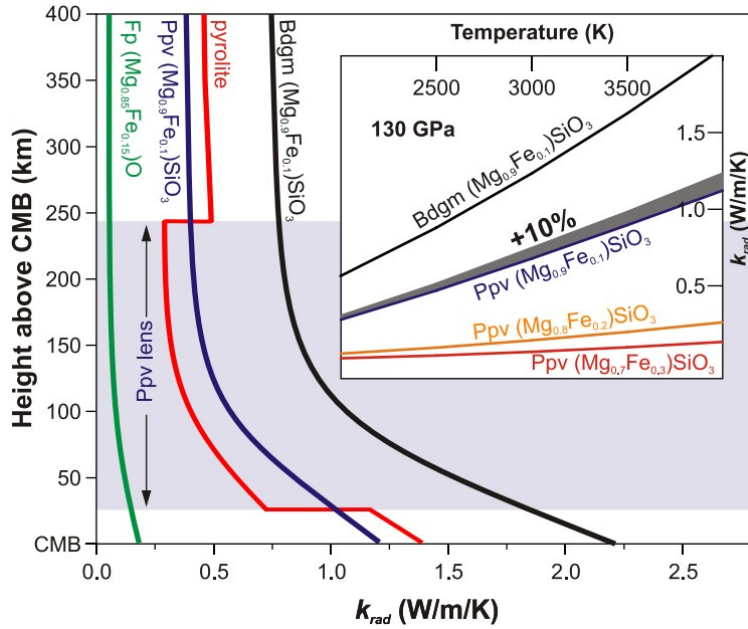


Figure 2. Radiative thermal conductivity (k_{rad}) of Ppv (dark blue) and Bdgm (black) with $Mg_{0.9}Fe_{0.1}SiO_3$ composition in the thermal boundary layer (TBL) along the intermediate geotherm of Ref.⁴. k_{rad} of Ppv was calculated using its absorption coefficient at 130 GPa reported by Goncharov et al.¹⁹ within the conventional formula (e.g. Ref.¹¹) and then corrected ($k_{rad} * 1.1$) for high temperature effects on the absorption coefficient. Pressure-dependence was neglected as it is weak over the relatively small pressure range of TBL. The overall uncertainty in k_{rad} is $\sim 25\%$ due to the ambiguity in the refractive index and sample thickness of Ppv. k_{rad} of Bdgm is based on the spectrum at 133 GPa and 300 K reported by Goncharov et al.¹¹ and was corrected for high-temperature effects ($k_{rad} * 1.1$). k_{rad} of Fp, $(Mg_{0.85}Fe_{0.15})O$, (green) is calculated based on the room-temperature spectrum at 133 GPa (Ref.¹³) and is not corrected for temperature effects. The red curve is the Hashin-Shtrikman averaged³² k_{rad} of a pyrolite composition (0.8 Bdgm or Ppv, and 0.2 Fp by volume). The kinked form of the red curve is due to the ‘double-crossing’³³ in the Ppv lens (gray area) assuming a temperature gradient of 7 K/km and a

CMB temperature of 4000 K. Inset: radiative conductivity of $Mg_{1-x}Fe_xSiO_3$ - Ppv for $x = 0.1$ (dark blue), $x = 0.2$ (orange), and $x = 0.3$ (red), respectively at 130 GPa. Blue-colored area shows the 10 % correction due to the temperature-dependent absorption coefficient.

Figure 2 shows a model of the radiative thermal conductivity in the lowermost mantle assuming a ~ 7 K/km temperature gradient, CMB temperature of 4000 K, and 10 % iron in Bdgm and Ppv (Ref.³⁴). According to the model, the ability of Ppv to conduct heat by radiation is ~ 40 % lower than that of Bdgm with a similar composition at expected CMB conditions of 135 GPa and 4000 K. The radiative conductivity of Ppv increases from ~ 0.35 at ~ 400 km above CMB to 1.2 W/m/K at CMB. Over the same depth interval, Bdgm k_{rad} increases from 0.75 to 2.2 W/m/K, while in Fp k_{rad} is < 0.2 W/m/K, a much lower value than that of Ppv and Bdgm. Radiative conductivity of Ppv, Bdgm, and Fp at CMB conditions is lower than the lattice thermal conductivity of their iron-free counterparts: 16.8 W/m/K (Ppv), 9 W/m/K (Bdgm), ~ 20 W/m/K (periclase) at corresponding conditions, according to experimental measurements using the thermorefectance method^{7, 35}. However, with increasing iron contents in these lower-mantle minerals, the lattice thermal conductivity is expected to decrease significantly due to the well-known phonon scattering effects in their lattices^{8, 35-37}, enhancing the role of the radiative thermal conductivity near CMB.

Combining the radiative conductivity model (**Fig. 2**) with the previously reported k_{lat} values of iron-free Bdgm and iron-free Ppv, we have constrained the total thermal conductivity of a pyrolytic mantle at near CMB conditions to 12.2 and 18.5 W/m/K for Bdgm- and Ppv-dominated rock, respectively. These values, however, are upper bounds on the thermal conductivity because the substitution of iron and/or aluminum in Ppv and Bdgm would inevitably decrease their k_{lat} by 10-50 % due to the phonon scattering effects (Refs.^{8, 13, 14, 35-37}). Accordingly, the total thermal conductivity is

$$k = \omega k_{lat}^{Fe-fr \text{ pyrolite}} + k_{rad}^{pyrolite} \quad (2)$$

where ω is the downward correction factor for k_{lat} in the pyrolite model due to the impurity-induced phonon scattering. The lattice and radiative components for the pyrolytic mantle can thus be modeled using the following equations:

$$k_{lat}^{pyrolite} = \omega z \langle 0.8k_{lat}^{Fe-free Ppv} + 0.2k_{lat}^{pericla\text{se}} \rangle + \omega(1-z) \langle 0.8k_{lat}^{Fe-free Bdgm} + 0.2k_{lat}^{pericla\text{se}} \rangle \quad (3)$$

$$k_{rad}^{pyrolite} = z \langle 0.8k_{rad}^{Ppv} + 0.2k_{rad}^{Fp} \rangle + (1-z) \langle 0.8k_{rad}^{Bdgm} + 0.2k_{rad}^{Fp} \rangle \quad (4)$$

where z is the abundance of Ppv, $z = V_{Ppv} / (V_{Ppv} + V_{Bdgm})$, where V_{Ppv} and V_{Bdgm} are the volumetric fractions of Ppv and Bdgm, respectively, and $\langle \ \rangle$ brackets denote the Hashin-Shtrikman averaging used to derive the effective conductivity of the mixture³². The fraction of Fp in the lower mantle is typically assumed to be on the order of 0.2 (Ref.³⁸) for a pyrolite mantle, but the global abundance and lateral variations in Ppv are largely unconstrained. Seismic studies have revealed patches at 200-400 km above the CMB with an S-wave velocity increase of a few percent that may be indicative of the presence of Ppv (Ref.³⁹). At the same time, it has been proposed that the pressure range of the Bdgm-Ppv transition is inconsistent with the depth of the D'' seismic discontinuity, questioning the presence of Ppv in the lowermost mantle^{40, 41}. It is thus of great interest to the deep-Earth community to constrain the abundance of Ppv in the TBL in order to evaluate the geodynamic consequences of the Bdgm-Ppv phase transition and the associated increase in the heat flow out of the core (Q_{CMB})^{3, 4, 33}.

Geodynamic modelling of the mantle and core has provided an estimate of $Q_{CMB} = 13 \pm 3$ TW (Ref.^{2, 39, 42}), which is related to the temperature gradient and thermal conductivity of the TBL by the Fourier law of heat conduction:

$$Q_{CMB} = A_{CMB} k \Delta T \quad (5)$$

where A_{CMB} is the surface area of the CMB and ΔT is the temperature gradient above the CMB. Substituting Eqn. (2) for k in Eqn. (5) and assuming an average temperature gradient of 7 K/km (Ref.³⁴) we can model the amount of Ppv in a pyrolytic mantle required to sustain the present-

day Q_{CMB} as a function of the downward correction factor (ω) to the lattice conductivity (Fig. 3). The values of the thermal conductivity for Ppv, Bdgm, and Fp used in our model are given in the Supplementary Table S1. Seismic data suggests that the distribution of Ppv in the lowermost mantle is highly non-uniform, with Ppv concentrated in large (up to 2000 km wide and ~ 200 km thick) lens-shaped structures^{3, 4, 39}. Accordingly, we applied the Hashin-Shtrikman averaging³² in Eqns. (3, 4) in order to model the thermal conductivity of pyrolytic mantle in the TBL layer (Fig. 3). The Hashin-Shtrikman approach proved adequate in determining the effective thermal conductivity of two-phase composites in the absence of detailed information on the spatial distribution of the phases³².

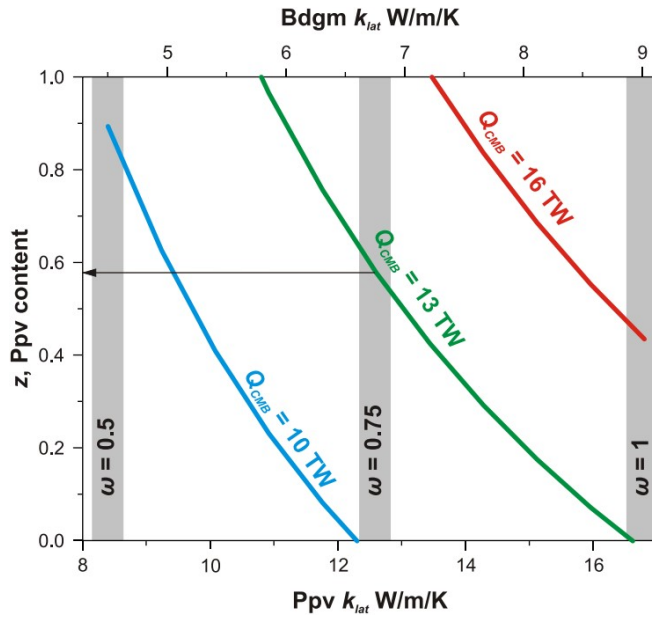


Figure 3. Ppv content in the thermal boundary layer (TBL) required to sustain the CMB heat flow of 10, 13, and 16 TW (blue, green, and red, respectively) for a given downward correction factor in the lattice conductivity ($\omega \leq 1$) at a temperature gradient of 7 K/km (see text for details). Ppv content (z) is defined as $z = [V_{Ppv} / (V_{Ppv} + V_{Bdgm})]$, where V_{Ppv} and V_{Bdgm} are the volumetric fractions of Ppv and Bdgm, respectively. Black arrow show the estimation of the Ppv content in the TBL assuming that the correction factor is at 25 % according to molecular dynamic simulations^{8, 37} and $Q_{CMB} = 13$ TW.

Our model suggests that Ppv should be present in the lowermost mantle to sustain 13 TW of the present-day CMB heat flow. For instance, a modest downward correction in the lattice

thermal conductivity ($\omega = 0.75$) for the pyrolite model requires $\sim 1:1$ ratio of Ppv and Bdgm (Fig. 3). The inferred abundance of Ppv is based on a model that does not rely on the highly uncertain parameters such as the depth and Clapeyron slope of the Bdgm-Ppv transition. Nonetheless, the derived volume ratio of Bdgm/Ppv of approximately 1 is consistent with the value derived from the analysis of the D'' seismic discontinuity in the region⁴³. The presence of such large portions of Ppv with relatively low thermal conductivity at the base of the lower mantle would result in mantle temperatures up to 500 K higher than that in a Ppv-free lowermost mantle, decreasing the buoyancy of plumes⁴⁴. Likewise, higher temperatures will reduce mantle viscosity amplifying the vigor of whole mantle convection and triggering small-scale convection in the TBL⁴⁵. If the lowermost mantle is enriched in iron, the downward correction in k_{lat} may be as large as 0.5 (Refs.^{35,36}), in which case the TBL must be dominated by Ppv even for the Q_{CMB} of 10 TW. On the other hand, $Q_{CMB} > 16$ TW demand that the whole TBL region is dominated by Ppv even for $\omega = 1$. However, the $Q_{CMB} < 10$ TW and $Q_{CMB} > 16$ TW scenarios are unlikely because they contradict mineral physics data on the impurity-dependence of lattice thermal conductivity of lower mantle minerals^{8,35-37}. Overall, our models show that most recent estimates of $Q_{CMB} = 13 \pm 3$ TW (Ref.^{2,39,42}) are consistent with the Ppv interpretation of the D'' seismic discontinuity. Future experimental and theoretical studies on the impurities effects on k_{lat} will enhance our understanding of the mineralogy and dynamical consequences of the Bdgm-Ppv phase transition of the CMB region.

Acknowledgements

This work was supported by the NSF Major Research Instrumentation program DMR-1039807, NSF EAR-1015239, NSF EAR-1520648 and NSF EAR/IF-1128867, the Army Research Office (56122-CH-H), the National Natural Science Foundation of China (grant number 21473211), the Chinese Academy of Sciences (grant number YZ201524), the Carnegie Institution of Washington and Deep Carbon Observatory. A. F. G. was partly supported by Chinese Academy of Sciences visiting professorship for senior international scientists (Grant No.

2011T2J20 and Recruitment Program of Foreign Experts. S.S.L. was partly supported by the Ministry of Education and Science of Russian Federation (No. 14.B25.31.0032). We acknowledge J. Liu, J. Yang, and V. Prakapenka for helping with the preparation and synthesis of the Ppv samples. The sample synthesis and XRD experiments were conducted at GSECARS 13IDD beamline of the Advanced Photon Source, Argonne National Laboratory.

GeoSoilEnviroCARS (Sector 13), Advanced Photon Source (APS), Argonne National Laboratory is supported by the National Science Foundation – Earth Sciences (EAR-1128799) and Department of Energy – GeoSciences (DE-FG02-94ER14466). This research used resources of the Advanced Photon Source, a U.S. Department of Energy (DOE) Office of Science User Facility operated for the DOE Office of Science by Argonne National Laboratory under Contract No. DE-AC02-06CH11357. J. F. Lin acknowledges support from the US National Science Foundation (EAR-1446946).

References and Notes

1. Lay, T., Hernlund, J., Buffett, B. A. Core-mantle boundary heat flow. *Nature Geosci.*, 1, 25-32 (2008).
2. Nimmo, F. in *Treatise on Geophysics (Second Edition)*, 27-55, (Oxford, 2015).
3. Lay, T., Hernlund, J., Garnero, E. J., Thorne, M. S. A post-perovskite lens and D " heat flux beneath the central Pacific. *Science*, 314, 1272-1276 (2006).
4. van der Hilst, R. D., *et al.* Seismostratigraphy and thermal structure of Earth's core-mantle boundary region. *Science*, 315, 1813-1817 (2007).
5. Murakami, M., Hirose, K., Kawamura, K., Sata, N., Ohishi, Y. Post-perovskite phase transition in MgSiO₃. *Science*, 304, 855-858 (2004).
6. Oganov, A. R. & Ono, S. Theoretical and experimental evidence for a post-perovskite phase of MgSiO₃ in Earth's D " layer. *Nature*, 430, 445-448 (2004).
7. Ohta, K., *et al.* Lattice thermal conductivity of MgSiO₃ perovskite and post-perovskite at the core-mantle boundary. *Earth Planet. Sci. Lett.*, 349, 109-115 (2012).
8. Ammann, M. W., *et al.* Variation of thermal conductivity and heat flux at the Earth's core mantle boundary. *Earth Planet. Sci. Lett.*, 390, 175-185 (2014).
9. Hofmeister, A. M. Mantle values of thermal conductivity and the geotherm from phonon lifetimes. *Science*, 283, 1699-1706 (1999).
10. Goncharov, A. F., Struzhkin, V. V., Jacobsen, S. D. Reduced radiative conductivity of low-spin (Mg,Fe)O in the lower mantle. *Science*, 312, 1205-1208 (2006).
11. Goncharov, A. F., Haugen, B. D., Struzhkin, V. V., Beck, P., Jacobsen, S. D. Radiative conductivity in the Earth's lower mantle. *Nature*, 456, 231-234 (2008).
12. Keppler, H., Dubrovinsky, L. S., Narygina, O., Kantor, I. Optical absorption and radiative thermal conductivity of silicate perovskite to 125 Gigapascals. *Science*, 322, 1529-1532 (2008).
13. Goncharov, A. F., Beck, P., Struzhkin, V. V., Haugen, B. D., Jacobsen, S. D. Thermal conductivity of lower-mantle minerals. *Phys. Earth Planet. Inter.*, 174, 24-32 (2009).
14. Goncharov, A. F., *et al.* Experimental study of thermal conductivity at high pressures: Implications for the deep Earth's interior. *Phys. Earth Planet. Inter.*, 247, 11-16 (2015).
15. Burns, R. G. *Mineralogical applications of crystal field theory*, (Cambridge University Press, U.K., 1993).
16. Lobanov, S. S., Goncharov, A. F., Litasov, K. D. Optical properties of siderite (FeCO₃) across the spin transition: Crossover to iron-rich carbonates in the lower mantle. *Am. Mineral.*, 100, 1059-1064 (2015).
17. Lobanov, S. S., Holtgrewe, N., Goncharov, A. F. Reduced radiative conductivity of low spin FeO₆-octahedra in FeCO₃ at high pressure and temperature. *Earth Planet. Sci. Lett.*, 449, 20-25 (2016).
18. Keppler, H., Kantor, I., Dubrovinsky, L. S. Optical absorption spectra of ferropericlase to 84 GPa. *Am. Mineral.*, 92, 433-436 (2007).
19. Goncharov, A. F., *et al.* Effect of composition, structure, and spin state on the thermal conductivity of the Earth's lower mantle. *Phys. Earth Planet. Inter.*, 180, 148-153 (2010).
20. McCammon, C. Perovskite as a possible sink for ferric iron in the lower mantle. *Nature*, 387, 694-696 (1997).
21. Sinmyo, R., Hirose, K., O'Neill, H. S., Okunishi, E. Ferric iron in Al-bearing post-perovskite. *Geophys. Res. Lett.*, 33, L12S13 (2006).
22. Mattson, S. M. & Rossman, G. R. Identifying characteristics of charge transfer transitions in minerals. *Phys. Chem. Miner.*, 14, 94-99 (1987).
23. Ismailova, L., *et al.* Stability of Fe,Al-bearing bridgmanite in the lower mantle and synthesis of pure Fe-bridgmanite. *Sci. Adv.*, 2, e1600427 (2016).
24. Lin, J. F., *et al.* Intermediate-spin ferrous iron in lowermost mantle post-perovskite and perovskite. *Nature Geosci.*, 1, 688-691 (2008).
25. Hsu, H., Yu, Y. G. G., Wentzcovitch, R. M. Spin crossover of iron in aluminous MgSiO₃ perovskite and post-perovskite. *Earth Planet. Sci. Lett.*, 359, 34-39 (2012).
26. Yu, Y. G. G., Hsu, H., Cococcioni, M., Wentzcovitch, R. M. Spin states and hyperfine interactions of iron incorporated in MgSiO₃ post-perovskite. *Earth Planet. Sci. Lett.*, 331, 1-7 (2012).
27. Ferguson, J., Guggenheim, H. J., Tanabe, Y. Absorption of light by pairs of like and unlike transition-metal ions. *Phys. Rev. Lett.*, 14, 737-738 (1965).
28. Smith, G. Evidence for absorption by exchange-coupled Fe²⁺-Fe³⁺ pairs in the near infra-red spectra of minerals. *Phys. Chem. Miner.*, 3, 375-383 (1978).

29. Lin, J.-F., *et al.* High-spin Fe²⁺ and Fe³⁺ in single-crystal aluminous bridgmanite in the lower mantle. *Geophys. Res. Lett.*, <http://dx.doi.org/10.1002/2016gl069836> (2016).
30. Holmstrom, E. & Stixrude, L. Spin crossover in ferropericlase from first-principles molecular dynamics. *Phys. Rev. Lett.*, 114, 117202 (2015).
31. Wall, A., Price, G. D., Parker, S. C. A computer simulation of the structure and elastic properties of MgSiO₃ perovskite. *Mineral. Mag.*, 50, 693-707 (1986).
32. Hashin, Z. & Shtrikman, S. A variational approach to theory of effective magnetic permeability of multiphase materials. *J. Appl. Phys.*, 33, 3125-3131 (1962).
33. Hernlund, J. W., Thomas, C., Tackley, P. J. A doubling of the post-perovskite phase boundary and structure of the Earth's lowermost mantle. *Nature*, 434, 882-886 (2005).
34. Stacey, F. D. & Davis, P. M. *Physics of the Earth*, (Cambridge University Press, Cambridge ; New York, 2008).
35. Dalton, D. A., Hsieh, W. P., Hohensee, G. T., Cahill, D. G., Goncharov, A. F. Effect of mass disorder on the lattice thermal conductivity of MgO periclase under pressure. *Sci. Rep.*, 3, 02400 (2013).
36. Manthilake, G. M., de Koker, N., Frost, D. J., McCammon, C. A. Lattice thermal conductivity of lower mantle minerals and heat flux from Earth's core. *Proc. Natl. Acad. Sci. U.S.A.*, 108, 17901-17904 (2011).
37. Stackhouse, S., Stixrude, L., Karki, B. B. First-principles calculations of the lattice thermal conductivity of the lower mantle. *Earth Planet. Sci. Lett.*, 427, 11-17 (2015).
38. Stixrude, L. & Lithgow-Bertelloni, C. Geophysics of chemical heterogeneity in the mantle. *Annu. Rev. Earth Planet. Sci.*, 40, 569-595 (2012).
39. Hernlund, J. W. & McNamara, A. K. in *Treatise on Geophysics (Second Edition)*, 461-519, (Oxford, 2015).
40. Catalli, K., Shim, S. H., Prakapenka, V. Thickness and Clapeyron slope of the post-perovskite boundary. *Nature*, 462, 782-785 (2009).
41. Grocholski, B., Catalli, K., Shim, S. H., Prakapenka, V. Mineralogical effects on the detectability of the postperovskite boundary. *Proc. Natl. Acad. Sci. U.S.A.*, 109, 2275-2279 (2012).
42. Gubbins, D., Alfe, D., Davies, C., Pozzo, M. On core convection and the geodynamo: Effects of high electrical and thermal conductivity. *Phys. Earth Planet. Iner.*, 247, 56-64 (2015).
43. Houser, C. in *Post-Perovskite: The Last Mantle Phase Transition*, 191-216, 2007).
44. Tosi, N., Yuen, D. A., de Koker, N., Wentzcovitch, R. M. Mantle dynamics with pressure- and temperature-dependent thermal expansivity and conductivity. *Phys. Earth Planet. Inter.*, 217, 48-58 (2013).
45. Samuel, H. & Tosi, N. The influence of post-perovskite strength on the Earth's mantle thermal and chemical evolution. *Earth Planet. Sci. Lett.*, 323, 50-59 (2012).

SUPPLEMENTARY MATERIALS AND METHODS

Methods

Absorption measurements in the visible (13000-22000 cm^{-1}) and infrared ranges (6200-11000 cm^{-1}) were divided into heating runs at two laser-heating systems equipped with different spectrometers and detectors (denoted hereafter as VIS and IR runs). A Leukos Pegasus pulsed supercontinuum light source (400-2400 nm) was inserted into the optical path of both systems, serving as a probe. For the VIS, the transmitted probe light was collected using a spectrometer with a 300 gr/mm grating and 300 nm focal length and a gated iCCD detector (Andor iStar SR-303i-A) synchronized with the supercontinuum pulses, identically to that described in Ref.¹. For the IR, we used Action Spectra Pro 2300i spectrometer equipped with a 150 gr/mm grating and an ungated InGaAs detector (Princeton Instruments Model 7498-0001). The collection of 2500 supercontinuum pulses over 10 ms was initiated 200 ms after the start of the 1 s laser heating. The large number of bright probe pulses in a short accumulation window was important to increase signal-to-noise ratio and suppress thermal background. The gap in absorption coefficients at $\sim 9000\text{-}10500 \text{ cm}^{-1}$ is due to the filters used to block the 1070 nm heating pulse, while the gap at $11000\text{-}13000 \text{ cm}^{-1}$ is due to the limited sensitivity of the iCCD and InGaAs detectors. The sample absorbance in these ranges was extrapolated based on the room temperature data collected with a conventional light source.

Double-sided laser-heating and temperature measurements in the VIS runs were identical to that of Ref.¹. For the IR runs, at double-sided laser-heating we could only perform single-sided temperature measurements for which the grating was centered at 1320 nm and the supercontinuum was blocked. In both VIS and IR, temperatures measurements were taken before and after the corresponding collection of the absorbance data at an identical laser power. The laser power was optimized to achieve comparable temperatures in the VIS and IR runs (within 50-100 K). Optical responses of the VIS and IR systems were calibrated using a standard white

lamp (Optronics Laboratories OL 220C). To extract the temperature, the emission spectra were fitted to the Planck black body function using the T-Rax software (C. Prescher). The reported temperature is an average of the VIS and IR measurements.

Sample thickness required to deduce the absorption coefficient of $\text{Mg}_{0.6}\text{Fe}_{0.4}\text{SiO}_3$ - Ppv was determined via white light interferometry at 130 GPa through the NaCl pressure medium. Additionally, the sample thickness was confirmed by direct SEM imaging of the recovered sample. The difference in sample thickness of $\sim 20\%$ between the two estimates is the main source of uncertainty in k_{rad} ($\sim 25\%$). Other contributions to the uncertainty include ambiguities in the refractive index of Ppv.

SUPPLEMENTARY TEXT

Valence and spin state of iron in $\text{Mg}_{0.6}\text{Fe}_{0.4}\text{SiO}_3$ post-perovskite (Ppv)

The interpretation of synchrotron-Mössbauer (SMS) and X-ray emission spectroscopy (XES) data on Ppv samples synthesized from polycrystalline enstatite with identical or closely-related composition²⁻⁴ is non-unique. However, density functional theory + Hubbard U allowed computing iron quadrupole splittings for Ppv⁵ that, in turn, allowed a consistent interpretation of the experimental data. Based on the combined theory-experiment view of the valence and spin state of iron in Ppv, we presume that iron in our $\text{Mg}_{0.6}\text{Fe}_{0.4}\text{SiO}_3$ Ppv is distributed between the A- ($\sim 70\%$ high-spin Fe^{2+} and $\sim 10\%$ high-spin Fe^{3+}) and B-sites ($\sim 20\%$ low-spin Fe^{3+}).

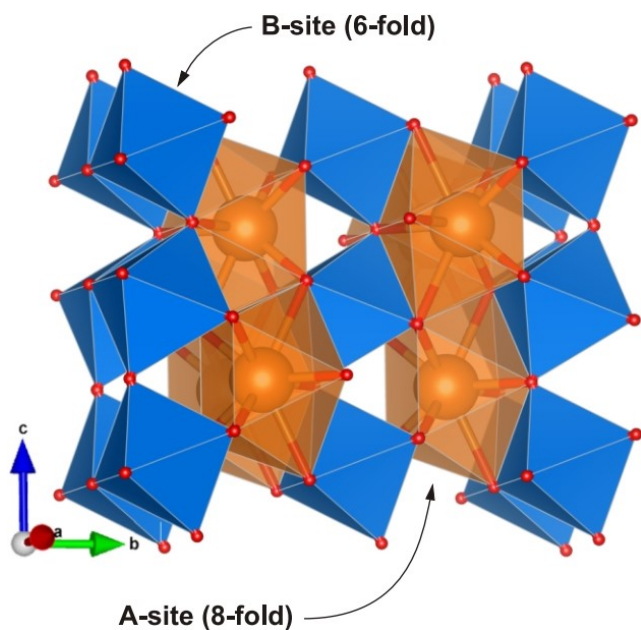
Band assignment in the absorption spectrum of $\text{Mg}_{0.6}\text{Fe}_{0.4}\text{SiO}_3$ Ppv

Our band assignment is consistent with the theory-experiment view in the presence of high spin Fe^{2+} in a weak crystal field (large A-site), the presence of both Fe^{2+} and Fe^{3+} in the synthesized sample, and low spin Fe^{3+} in a strong crystal field (small B-site).

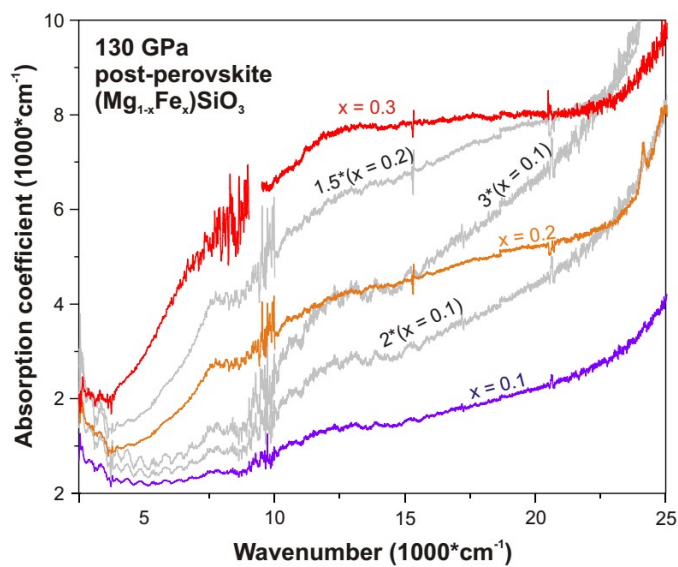
Specifically, ${}^5E_g \rightarrow {}^5T_{2g}$ in Fe^{2+} transitions at 6-folded sites (stronger crystal field) typically show energies of 10000-12000 cm^{-1} , while in bridgmanite a 12-folded (weaker crystal field) HS Fe^{2+} has a ${}^5E_g \rightarrow {}^5T_{2g}$ transition at ~ 7000 cm^{-1} (Ref.⁶). Accordingly, we assign the band centered at ~ 7500 cm^{-1} to the ${}^5E_g \rightarrow {}^5T_{2g}$ in Fe^{2+} at the A-site.

Tanabe-Sugano diagram for Fe^{3+} at the B-site (Supplementary Fig. S3) is consistent with the assignment of the band at ~ 17500 cm^{-1} to the ${}^2T_{2g} \rightarrow {}^2T_{1g}$ (${}^2A_{2g}$) transition in LS Fe^{3+} . The assignment can be tested by supposing the Racah parameter B of 600 cm^{-1} (Refs.^{7,8}). The ${}^2T_{1g}$ (${}^2A_{2g}$) state has an energy of 22B at the HS to LS transition, while the energy of the 2E_g state is significantly higher ($\sim 29B$ at the spin transition). Accordingly, we obtain frequencies of 13200 and 17400 cm^{-1} for the two lowest energy excited states at the spin transition pressure, which was theoretically predicted to be at ~ 30 GPa (Ref.⁵). Assuming a reasonable blue-shift of 30-90 cm^{-1}/GPa (Ref.^{9,10}) we obtain 16200-22200 and 20400-26400 cm^{-1} for the ${}^2T_{1g}$ (${}^2A_{2g}$) and 2E_g bands, respectively. Therefore, the band centered at 17500 cm^{-1} can only be assigned to the ${}^2T_{2g} \rightarrow {}^2T_{1g}$ (${}^2A_{2g}$) transition in LS Fe^{3+} .

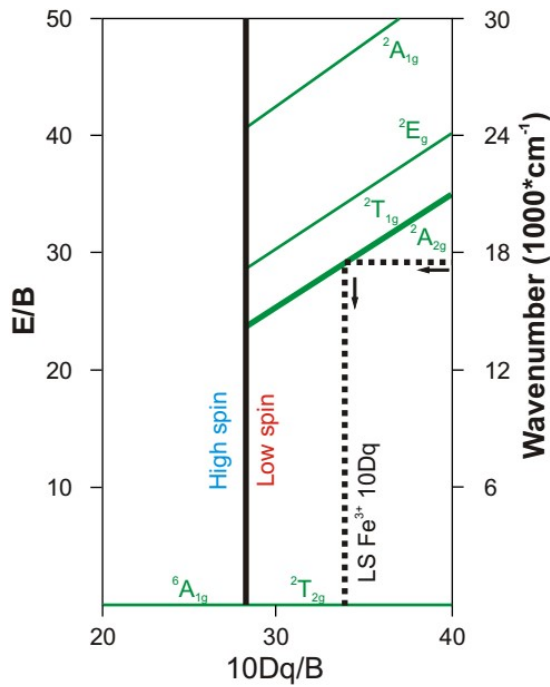
SUPPLEMENTARY FIGURES



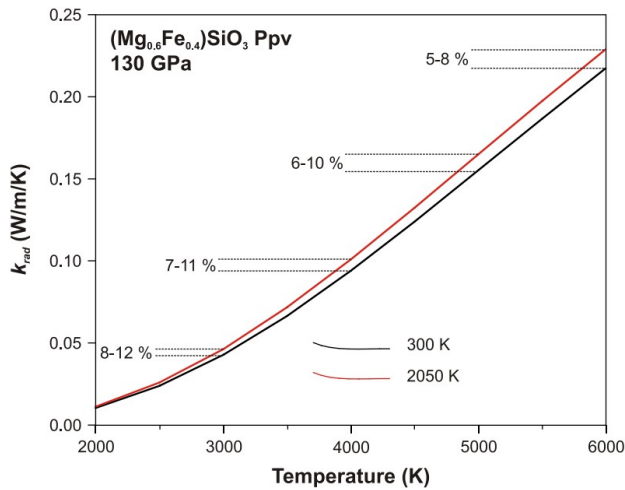
Supplementary Figure S1. Post-perovskite crystal structure. A-site is shown by orange polyhedrons with spheres and B-site by blue octahedra. Small red spheres represent oxygen atoms.



Supplementary Figure S2. Absorption coefficients of $\text{Mg}_{1-x}\text{Fe}_x\text{SiO}_3$ - Ppv for $x=0.1$ (purple), $x=0.2$ (orange), and $x=0.3$ (red), respectively (after Ref.¹¹). Grey curves depict absorption coefficients of Ppv with $x=0.1$ and $x=0.2$ multiplied by 2 and 3 (for $x=0.1$), and by 1.5 (for $x=0.2$) for better comparison.



Supplementary Figure S3. Tanabe-Sugano diagram for d^5 elements in 6-fold coordination. Green lines depict spin-allowed transitions as a function of the crystal field splitting energy ($10Dq$). The Racah parameter B is assumed to be 600 cm^{-1} as the reported values are $B \sim 590\text{--}650\text{ cm}^{-1}$ for Fe^{3+} in 6-fold coordination⁸. Note that ${}^2T_{1g}$ and ${}^2A_{2g}$ excited states have identical energies. We evaluate the crystal field splitting energy of LS Fe^{3+} as $10Dq = 20350\text{ cm}^{-1}$ (the procedure is shown by the thick dotted line).



Supplementary Figure S4. Radiative thermal conductivity of $\text{Mg}_{0.6}\text{Fe}_{0.4}\text{SiO}_3$ - Ppv at 130 GPa evaluated using absorption coefficients shown in Fig.1 for different sample temperatures. The difference in k_{rad} evaluated from the absorption spectrum at 2050 K is 5-12 % higher than that evaluated from the spectra at 300 K.

SUPPLEMENTARY TABLES

Supplementary Table S1. Lattice and radiative thermal conductivities of major lower mantle minerals at expected core-mantle boundary conditions. The values used in the modelling are shown in bold.

| Phase | Mechanism | k, W/m/K | P, GPa / T, K | Composition | Source | Method |
|----------------------------------|------------------|-------------------|-------------------------|--|--------------------------|--|
| Post-perovskite | lattice | 16.8 ± 3.7 | 135 GPa / 3700 K | MgSiO₃ | Ref.¹² | Thermoreflectance |
| Post-perovskite | lattice | 15.1 ± 0.9 | 140 GPa / 3000 K | MgSiO ₃ | Ref. ¹³ | <i>ab initio</i> |
| Post-perovskite | lattice | 10.7 | 135 GPa / 4000 K | MgSiO ₃ | Ref. ¹⁴ | <i>ab initio</i> |
| <hr/> | | | | | | |
| Bridgmanite | lattice | 9.0 ± 1.6 | 135 GPa / 3700 K | MgSiO₃ | Ref.¹² | Thermoreflectance |
| Bridgmanite | lattice | 2.3 | 100 GPa / 4000 K | MgSiO ₃ | Ref. ¹⁵ | <i>ab initio</i> |
| Bridgmanite | lattice | 1.6 | 136 GPa / 4000 K | MgSiO ₃ | Ref. ¹⁶ | <i>ab initio</i> |
| Bridgmanite | lattice | 6.8 ± 0.9 | 136 GPa / 4000 K | MgSiO ₃ | Ref. ¹⁷ | <i>ab initio</i> |
| Bridgmanite | lattice | 12.4 ± 2.0 | 137 GPa / 3000 K | MgSiO ₃ | Ref. ¹³ | <i>ab initio</i> |
| Bridgmanite | lattice | 7.9 | 135 GPa / 4000 K | MgSiO ₃ | Ref. ¹⁴ | <i>ab initio</i> |
| <hr/> | | | | | | |
| Periclase, single crystal | lattice | 21.5 ± 5 | 135 GPa / 3700 K | MgO | Ref.¹⁸ | Thermoreflectance |
| Periclase, powder | lattice | 17.9 ± 1.1 | 135 GPa / 3600 K | MgO | Ref. ¹⁹ | Thermoreflectance |
| Periclase | lattice | 20 ± 5 | 136 GPa / 4100 K | MgO | Ref. ²⁰ | <i>ab initio</i> |
| <hr/> | | | | | | |
| Post-perovskite | radiative | 1.2 ± 0.2 | 130 GPa / 4000 K | Mg_{0.9}Fe_{0.1}SiO₃ | This study | Optical absorption at high T |
| Bridgmanite | radiative | 2.2 ± 0.4 | 133 GPa / 4000 K | Mg_{0.9}Fe_{0.1}SiO₃ | This study | Optical absorption at 300 K, corrected for high T |
| Ferropericlase | radiative | 0.2 ± 0.1 | 133 GPa / 4000 K | Mg_{0.85}Fe_{0.15}O | This study | Optical absorption at 300 K |

References and Notes

1. Lobanov, S. S., Holtgrewe, N., Goncharov, A. F. Reduced radiative conductivity of low spin FeO₆-octahedra in FeCO₃ at high pressure and temperature. *Earth Planet. Sci. Lett.*, 449, 20-25 (2016).
2. Lin, J. F., *et al.* Intermediate-spin ferrous iron in lowermost mantle post-perovskite and perovskite. *Nature Geosci.*, 1, 688-691 (2008).
3. Mao, Z., *et al.* Electronic spin and valence states of Fe in CaIrO₃-type silicate post-perovskite in the Earth's lowermost mantle. *Geophys. Res. Lett.*, 37, L22304 (2010).
4. Lin, J. F., Speziale, S., Mao, Z., Marquardt, H. Effects of the electronic spin transitions of iron in lower mantle minerals: implications for deep mantle geophysics and geochemistry. *Rev. Geophys.*, 51, 244-275 (2013).
5. Yu, Y. G. G., Hsu, H., Cococcioni, M., Wentzcovitch, R. M. Spin states and hyperfine interactions of iron incorporated in MgSiO₃ post-perovskite. *Earth Planet. Sci. Lett.*, 331, 1-7 (2012).
6. Keppler, H., Mccammon, C. A., Rubie, D. C. Crystal-field and charge-transfer spectra of (Mg,Fe)SiO₃ perovskite. *Am. Mineral.*, 79, 1215-1218 (1994).
7. Sherman, D. M. & Waite, T. D. Electronic spectra of Fe³⁺ oxides and oxide hydroxides in the near IR to near UV. *Am. Mineral.*, 70, 1262-1269 (1985).
8. Burns, R. G. *Mineralogical applications of crystal field theory*, (Cambridge University Press, U.K., 1993).
9. Keppler, H., Kantor, I., Dubrovinsky, L. S. Optical absorption spectra of ferroperricite to 84 GPa. *Am. Mineral.*, 92, 433-436 (2007).
10. Lobanov, S. S., Goncharov, A. F., Litasov, K. D. Optical properties of siderite (FeCO₃) across the spin transition: Crossover to iron-rich carbonates in the lower mantle. *Am. Mineral.*, 100, 1059-1064 (2015).
11. Goncharov, A. F., *et al.* Effect of composition, structure, and spin state on the thermal conductivity of the Earth's lower mantle. *Phys. Earth Planet. Inter.*, 180, 148-153 (2010).
12. Ohta, K., *et al.* Lattice thermal conductivity of MgSiO₃ perovskite and post-perovskite at the core-mantle boundary. *Earth Planet. Sci. Lett.*, 349, 109-115 (2012).
13. Haigis, V., Salanne, M., Jahn, S. Thermal conductivity of MgO, MgSiO₃ perovskite and post-perovskite in the Earth's deep mantle. *Earth Planet. Sci. Lett.*, 355, 102-108 (2012).
14. Ammann, M. W., *et al.* Variation of thermal conductivity and heat flux at the Earth's core mantle boundary. *Earth Planet. Sci. Lett.*, 390, 175-185 (2014).
15. Dekura, H., Tsuchiya, T., Tsuchiya, J. Ab initio lattice thermal conductivity of MgSiO₃ perovskite as found in Earth's lower mantle. *Phys. Rev. Lett.*, 110, 025904 (2013).
16. de Koker, N. Thermal conductivity of MgO periclase at high pressure: Implications for the D " region. *Earth Planet. Sci. Lett.*, 292, 392-398 (2010).
17. Stackhouse, S., Stixrude, L., Karki, B. B. First-principles calculations of the lattice thermal conductivity of the lower mantle. *Earth Planet. Sci. Lett.*, 427, 11-17 (2015).
18. Dalton, D. A., Hsieh, W. P., Hohensee, G. T., Cahill, D. G., Goncharov, A. F. Effect of mass disorder on the lattice thermal conductivity of MgO periclase under pressure. *Sci. Rep.*, 3, 02400 (2013).
19. Imada, S., *et al.* Measurements of lattice thermal conductivity of MgO to core-mantle boundary pressures. *Geophys. Res. Lett.*, 41, 4542-4547 (2014).
20. Stackhouse, S., Stixrude, L., Karki, B. B. Thermal conductivity of periclase (MgO) from first principles. *Phys. Rev. Lett.*, 104, 208501 (2010).